ACS APPLIED MATERIALS & INTERFACES

Research Article

www.acsami.org

Porous Three-Dimensional Flower-like Co/CoO and Its Excellent Electromagnetic Absorption Properties

Hualiang Lv,[†] Xiaohui Liang,[†] Guangbin Ji,*[,†] Haiqian Zhang,[†] and Youwei Du[‡]

[†]College of Materials Science and Technology, Nanjing University of Aeronautics and Astronautics, Nanjing 210016, Peoples Republic of China

[‡]Laboratory of Solid State Microstructures, Nanjing University, Nanjing 210093, Peoples Republic of China

ABSTRACT: The porous three-dimensional (3-D) flower structures assembled by numerous ultrathin flakes were favor for strengthen electromagnetic absorption capability. However, it still remains a big challenge to fabricate such kind of materials. In this study, an easy and flexible two-step method consisting of hydrothermal and subsequent annealing process have been developed to synthesize the porous 3-D flower-like Co/CoO. Interestingly, we found that the suitable heat treatment temperature played a vital role on the flower-like structure, composition, and electromagnetic absorption properties. In detail, only in the composite treated with 400 °C can we gain the porous 3-D flower structure. If the annealing temperature were heated to 300 °C, the Co element was unable to generate. Moreover, when the annealing temperature increased from 400 to 500 °C, these flower-like structures were unable to be kept because the enlarged porous diameter would wreck the flower frame. Moreover, these 3-D porous flower-like structures presented outstanding electromagnetic absorption properties. For example, such special structure enabled an optimal reflection loss value of −50 dB with the frequency bandwidth ranged from 13.8 to 18 GHz. The excellent microwave absorption performance may attribute to the high impedance matching behavior and novel dielectric loss ability. Additionally, it can be supposed that this micrometer-size flower structure was more beneficial to scatter the incident electromagnetic wave. Meanwhile, the rough surface of the ultrathin flake is apt to increase the electromagnetic scattering among the leaves of the flower due to their large spacing and porous features.

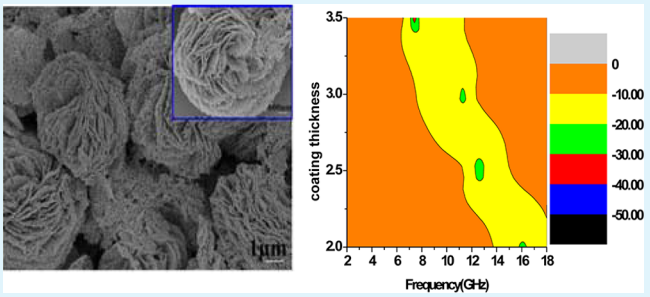

KEYWORDS: *porous 3-D flower structure, Co/CoO, electromagnetic absorption properties, impedance matching, lightweight*

1. INTRODUCTION

Arising from the rapid development of electronic devices, wireless communication tools, and local area networks, electromagnetic interference (EMI) has greatly threatened human health and disturbed various commercial or industrial equipment.[1−3] Thus, the demand for electromagnetic absorbents has become urgent over the past years. It is well-known that an electromagnetic absorbent is a type of functional material that is able to absorb incidence of electromagnetic wave effectively and then convert it into thermal energy.[4,5] The ideal absorbing materials must have light weight, strong absorption, thin thickness, and broad frequency.[6] Several factors, such as morphology, geometry and microstructure, are crucial in determining the electromagnetic absorption properties.[7] Currently, different morphologies of absorbents have been fabricated by various methods, containing one-dimensional (1-D; nanowires, nanoparticles),[8−11] two-dimensional (2-D; flake, nanodisks)[12,13] and three-dimensional (3-D; tubes, sphere, urchin-like structure).[14−18] For example, SiC nanowires with 20−80 nm in diameter, several tens of micrometers in length have been developed by reducing the multiwall carbon nanotubes (MWCNTs) and silicon vapor from molten salt medium. The minimum reflection loss value (RL_{min}) reached as high as −17.4 dB at a coating thickness of 4 mm.[19] Meanwhile, the well-defined hexagonal flake-shape iron with a thickness of about 100−500 nm and edge length of 5 μm has been produced by hydrogen reduction of α-Fe_2O_3 microflakes, and the optimal reflection value was up to 15.3 dB.[20] Sun et al. compared the electromagnetic absorption performance of CoO nanobelts, submicrometer spheres, and bulks and found that the nanobelts have the highest reflection loss value of −12.3 dB at a thickness of 3 mm.[21] Therefore, we conclude that these shapes of absorbent with different sizes and crystal structures have a vital influence on the electromagnetic absorption that may result from electronic polarization, magnetic loss, and so on. Considerable attention has been focused on the monodispersed flower shape of absorbing materials due to its fascinating advantages. Generally, most of the microwave absorbents have difficulties in improving the permeability in high frequency regions because of its large eddy current (the strong magnetic field induced by the eddy current can cancel the external magnetic field and cause low

Received: February 21, 2015
Accepted: April 16, 2015
Published: April 16, 2015

DOI: 10.1021/acsami.5b01654
ACS Appl. Mater. Interfaces 2015, 7, 9776−9783

permeability and poor microwave absorption).[22,23] However, some reports pointed out that the absorbing materials with flake-like structures can efficiently suppress the eddy current due to its high resonance peak at a high frequency range.[24] A 3-D flower structure consisting of numerous flake-shaped structures has been regarded as a promising microwave-absorbing material. More importantly, the special 3-D structure may scatter the electromagnetic wave among the layers of flower and increase the microwave absorption properties. Various flower-shaped absorbing materials have been successfully synthesized, such as Ni with a RL_{min} value of −17 dB at 13 GHz,[25] FeNi@C with a RL_{min} value of −47.6 dB at 3.17 GHz.[26] But, these flower-shaped absorbing materials consist of a high density of cobalt or nickel, which is not beneficial for lightweight microwave absorbing material. In order to solve this problem, porous materials are regarded as an effective way to meet the demand of light absorption.[27−29]

In this study, we designed a novel porous 3-D flower-like Co/CoO structure as a new type of microwave absorption materials. These well-defined flower structures consist of numerous large ultrathin flakes, which exceed the Snoek limitation. At the same time, the porous structure with a lower density can be used as lightweight microwave absorption material. In additional, the layer spacing of the flakes in each flower structure is relatively favorable for electromagnetic scattering.

2. EXPERIMENTAL SECTION

2.1. Materials. Cobalt acetate ($Co(OAc)_2$), urea, and polyvinylpyrrolidone (PVP, K30) were purchased from Nanjing Chemical Reagent Co. Methanol were purchased from the Sinopharm Chemical Reagent Co. All of the chemical reagents were analytically pure and used without further purification.

2.2. Preparation of Porous Flower-Shaped Co/CoO Composite. The flower-shaped Co/CoO composite was prepared by a simple solvothermal approach. The typical experimental procedure is as follows: 0.5 g of polyvinylpyrrolidone (PVP) was dissolved in 50 mL of methanol under magnetic stirring for 10 min. Then, 0.5 g of cobalt acetate and 0.25 g of urea were added into the solution and ultrasonic treated for 20 min to form a clear red solution. Subsequently, the mixed solution was transferred into a Teflon-lined stainless steel autoclave with a capacity of 100 mL. The hydrothermal process was carried out at 200 °C for 6 h, and then the mixture was allowed to cool to ambient temperature. The final products were washed with ethanol. Finally, the product was dried in a vacuum at a temperature of 60 °C. In the second stage, 0.1 g of the as-prepared precursor was heated at 400 °C/500 °C (marked in S1 and S2) for 2 h with a slow increase rate of 1 °C/min and with nitrogen gas (N_2) as the protective gas.

2.3. Characterizations. Phase analysis was tested by the powder X-ray diffraction (XRD) patterns (Bruker D8 ADVANCE X-ray diffractometer) using Cu Kα radiation (λ = 0.154178 nm with 40 kV scanning voltage, 40 mA scanning current. A Hitachi S4800 type scanning electron microscopy (operated at an acceleration voltage of 3.0 kV and equipped with an energy dispersive X-ray spectroscopy) were used to observe the morphology features and sizes. The morphology of the composite was further characterized by transmission electron microscope (TEM, JEM JEOL 2100). The magnetic properties including coercive force and saturation magnetization were performed by a vibrating sample magnetometer (VSM, Lakeshore, Model 7400 series) at room temperature. The XPS spectrum was measured in a PHI 5000 VersaProbe systems using an Al Kα X-ray source and operating at 150 W. The Brunauer−Emmett−Teller (BET, ASAP2020) was utilized to analysis the specific surface and pore size. The S parameters including S11, S12, S21, and S22 will be tested by an Agilent PNA N5224A vector network analyzer using the coaxial-line method which the samples prepared by homogeneously mixing the paraffin wax and sample (mass ratio was 1:1) and then pressing into toroidal-shaped samples (Φ_{out}, 7.0 mm; Φ_{in}, 3.04 mm). Afterward, software which has been installed in Agilent PNA can calculate the ε', ε'', μ', and μ'' values. Finally, the RL value with different thickness can be calculated by using the following formulas.[30,31]

$$Z_{in} = Z_0\sqrt{\mu_r/\varepsilon_r}\ \tan h\ [j(2\pi fd/c)]\ \sqrt{\mu_r\varepsilon_r} \quad (1)$$

$$\mathrm{RL}(dB) = 20\log|(Z_{in} - Z_0)/(Z_{in} + Z_0)| \quad (2)$$

where Z_{in} is the input impedance of the absorber; f is the frequency of electromagnetic wave, d is the coating thickness of the absorber; c is the velocity of electromagnetic wave in free space; and ε_r ($\varepsilon_r = \varepsilon' - j\varepsilon''$) and μ_r ($\mu_r = \mu' - j\mu''$) are the complex permittivity and permeability of the absorber, respectively.

3. RESULTS AND DISCUSSION

3.1. Morphology and Microstructure of Precursor. During the solvothermal process, the precursor salt ($Co(OAc)_2$) can be divided into two reaction process under alkaline solution, as expressed in the following:

$$Co(CH_3COO)_2 + 2OH^- = Co(OH)_2 + 2CH_3COO^- \quad (1)$$

$$Co(CH_3COO)_2 = CoC_2O_4 + C_2H_6 \quad (2)$$

It is worth pointing out that for reaction 2, decomposition of $Co(CH_3COO)_2$ should satisfy the conditions of high temperature and high pressure. During the solvothermal process, the sealed autoclave with a high temperature of 200 °C may generate the high pressure and thus result in the occurring of reaction 2.

Derived from the XRD patterns analysis of the precursor, it is found from Figure 1a that these strong diffraction peaks at 22.2, 32.7, 33.3, 37.7, 45.1, 50.9 and 58.2° can be easily ascribed to the crystal planes of $Co(OH)_2$ (JCPDS card No. 02-0925).[32] In fact, the color of pure $Co(OH)_2$ presents pink while the as-prepared precursor appearing in this study is slight dark (Figure 1a, inset), demonstrating that the precursor is not single component and may still exist the CoC_2O_4. Nevertheless, there is still no distinct evidence to prove the presence of crystalline CoC_2O_4 just from the XRD patterns due to its probable amorphous state. Herein, further measurements, including energy disperse spectroscopy (EDS) and Fourier transform infrared (FT-IR), are carried out to analyze the composition. First, the EDS spectrum shows the presence of Co, O, and C elements, which proves the probable presence of CoC_2O_4 (Figure 1b). (Before EDS, the sample was put in the single-crystal Si substrate to rule out the C element coming from the conductive adhesive). Subsequently, the precursor was tested by the FT-IR spectrum as displayed in Figure 1c. Obviously, the wavenumbers at 1065, 1160−1460, and 1630 cm^{-1} belong the C−C, O−C═ and C═O bands, suggesting the presence of CoC_2O_4. Thus, we may deduce that the as-prepared precursor is composed of $Co(OH)_2$ and CoC_2O_4. In additional, the wavenumber at around 586 cm^{-1} is attributed to the characterization vibrating peak of $Co(OH)_2$ and is consistent with the XRD result.

The morphology feature of the precursor was displayed in Figure 2. It can be seen that the precursor presents 3-D flower-like shape, and the size of monodisperse flower structure is within a narrow region of 2−4 μm. Further magnifying the flower reveals that the flower-like structure consists of numerous smooth ultrathin-sheet structures with uniformly thickness of about 20 nm. From the element mappings of Figure 2(c−f), we can observe that the C, O, and Co is

DOI: 10.1021/acsami.5b01654
ACS Appl. Mater. Interfaces 2015, 7, 9776−9783

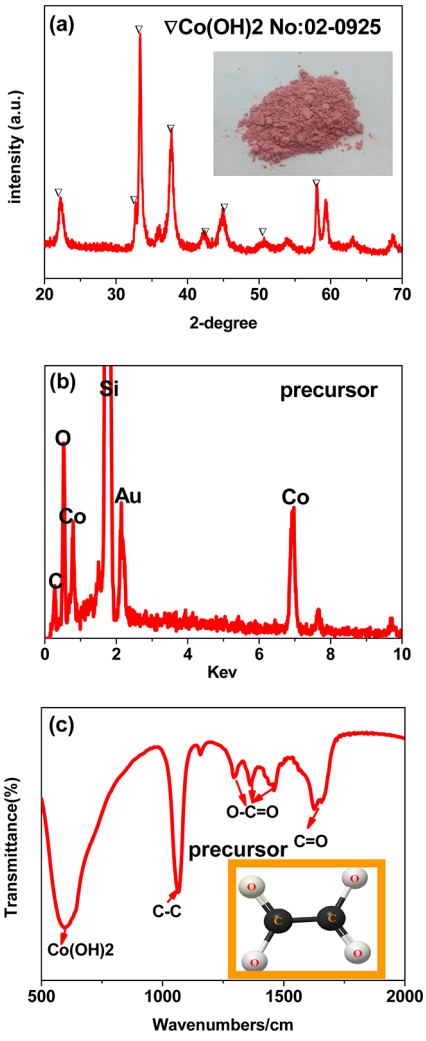

Figure 1. (a) XRD patterns (b) EDS and (c) FT-IR spectra of the as-prepared flower-like precursor; (a, inset) photograph of the as-prepared precursor.

uniformly distributed in the flower structure, whereas the density of C is less dense than that of Co and O element, meaning the mass ratio of CoC_2O_4 is less than $Co(OH)_2$.

3.2. Morphology and Microstructure of the Co/CoO. The Co/CoO composite is prepared by a simple heat treatment process under the flowing nitrogen gas, and the temperature is set at 300 to 500 °C for 2 h, respectively. As shown in Figure 3, there are six main diffraction peaks located at 36.5, 42.6, 44.2, 51.1, 61.6, and 75.8° in S1 and S2, which can be assigned to the (111), (200), and (220) crystal planes of CoO (JCPDS card No. 65-2902) and (111), (200), and (211) of Co (JCPDS card No. 15-0806), respectively. However, it should be pointed out that the Co diffraction peaks are not present in the sample prepared at 300 °C. The Co diffraction peaks of S2 are obviously strong. As a result, we deduce that the apparent increase of Co diffraction peaks intensity may be caused by the increased mass of Co in the composite. Such a phenomenon can be explained by the following. When the precursor under the heat treatment process, a series of reactions is acquired as expressed in the following equations:

$$Co(OH)_2 = CoO + H_2O \quad (3)$$

$$CoC_2O_4 = CoO + CO + CO_2 \quad (4)$$

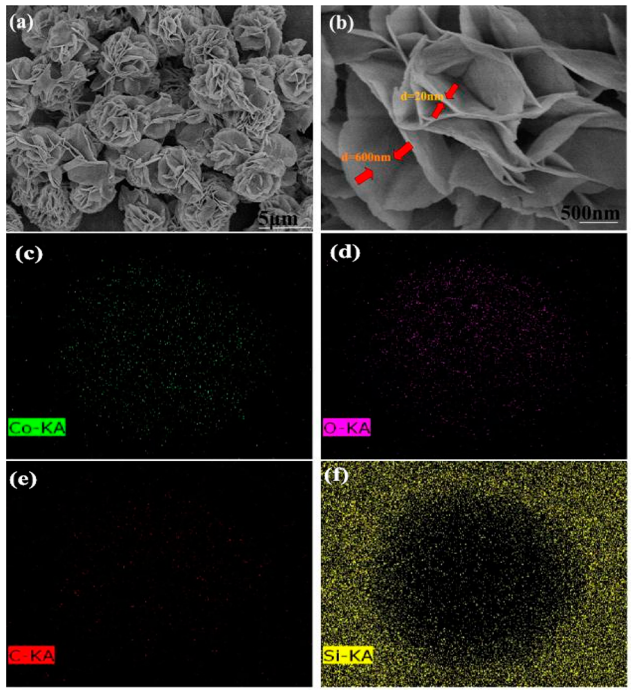

Figure 2. (a and b) SEM images and (c–f) elements mapping of the flower-like precursor.

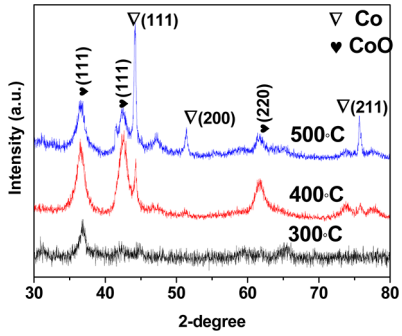

Figure 3. XRD patterns of the Co/CoO prepared at 300–500 °C.

$$CoO + CO = Co + CO_2 \quad (5)$$

It is clearly observed that the metal Co results from the decomposition of CoC_2O_4. For reaction 4, it is an endothermic process, so the equilibrium constant, K, increases as the temperature constantly increases, and more and more CO is generated as the temperature increases from 400 to 500 °C. Afterward, the CoO is reduced to Co. Such a result is consistent with XRD patterns and the magnetic properties (see below). However, reaction 5 still needs a relatively high temperature, although it is an exothermal process ($\Delta H = -45.1$ kJ/mol < 0), which can explain why we cannot achieve Co element at a lower temperature of 300 °C.

The X-ray photoelectron spectrum was also performed to analyze the form of Co. As shown in Figure 4, the binding energy values of Co $2p_{3/2}$ are located at 780.1 and 778.6 eV, which can be corresponded to CoO and Co, respectively.[33,34] To test the weight ratio, we used a facile hydrogen gas reduction (reduce CoO to Co and the loss weight is represent for the O element resulting from the CoO) and the result indicates that the Co weight ratio is 34.2 wt % for S1 and 39.2 wt % for S2, respectively.

DOI: 10.1021/acsami.5b01654
ACS Appl. Mater. Interfaces 2015, 7, 9776–9783

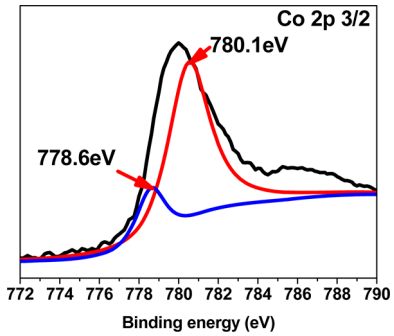

Figure 4. XPS spectra of the porous 3-D flower-like precursor.

Figure 5 reveals the FE-SEM and TEM images of the Co/CoO composites. It is noted from Figure 5a,b that S1 still

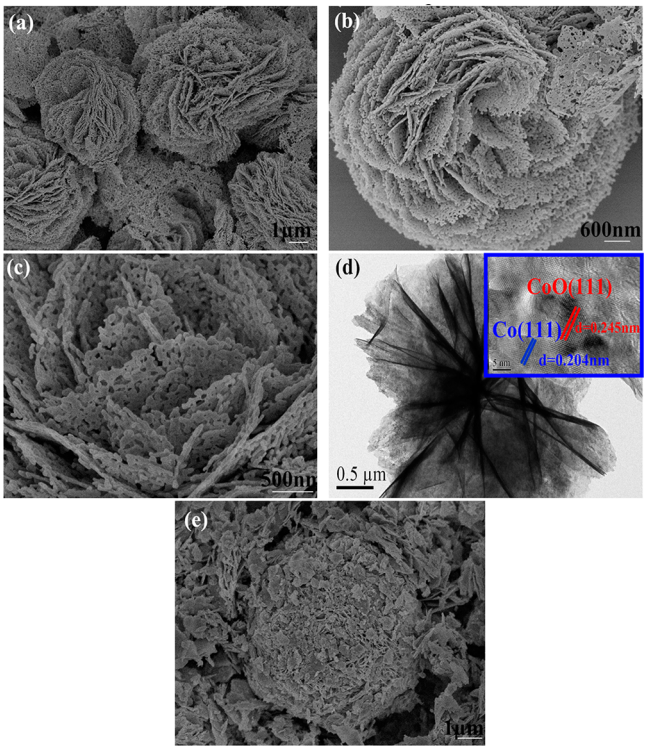

Figure 5. (a–c) SEM images of the porous 3-D flower-like Co/CoO at different magnification (prepared at 400 °C), (d) HR-TEM image of the porous 3-D flower structure (prepared at 400 °C), and (e) SEM image of the sample prepared at 500 °C.

maintains its special flower shape. However, the porous structure originates from the loss of H_2O; O then left empty spaces as the pores in the leaf of the flower structure. The HR-TEM image selected from the leaf of the flower structure suggests that there are two types of lattice spacing; one is 0.245 nm, corresponding to (111) crystal plane of CoO, while the other is 0.204 nm, ascribing to (111) crystal plane of Co element. This consequence demonstrates the presence of Co and CoO (Figure 5d and inset). When the temperature was further increased to 500 °C, the porous flower shapes collapsed, and numerous ultrathin flakes without regular morphology emerged (Figure 5e). That can be explained that as the temperature increased further, the size of the pores would enlarge due to the exceeding reduction of CoO and the loss of more O elements. Finally, the enlargement of porous size could not support the frame of the flower structure and resulted in collapse.

The BET date (Figure 6) implies that the specific surface area (S_{BET}) of both the samples (sample S1 and S2) is not

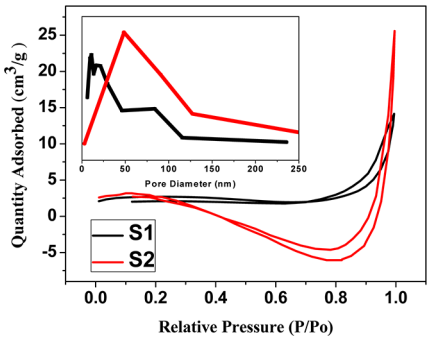

Figure 6. N_2 adsorption–desorption isotherms of the porous 3-D flower-like Co/CoO; (inset) pore size distribution plots.

large; the S_{BET} of S1 is about 9.2 m^2/g, slightly higher than the S_{BET} of S2, 8.44 m^2/g. Such small S_{BET} values may attribute to the micrometer sizes of S1 and S2. However, the pore size of S2 was mainly around 65 nm, which is bigger than the 25 nm of S1 pores. The result further demonstrates that after increasing the heating temperature, a small part of CoO reduced and led to the enlargement of the pore size.

The hysteresis loss has been measured at room temperature by the vibrating sample magnetometer (VSM). From Figure 7,

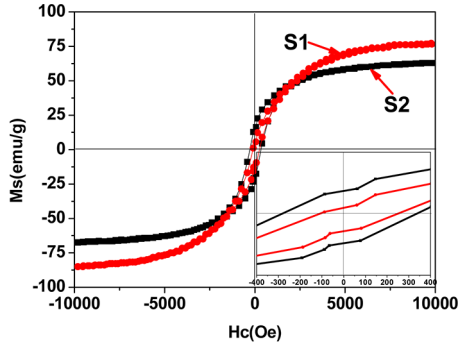

Figure 7. Hysteresis loop of the Co/CoO prepared at 400 (S1) and 500 °C (S2).

it is not difficult to find that S2 has a higher magnetization value of about 76 emu/g, while that of S1 is about 62 emu/g. In addition, S1 exhibits a higher coercive force value (H_c; 309.64 Oe) than that of S2 (178.75 Oe). It is worth noting that a large H_c value is always benefic for high-frequency resonance based on the following equation:[35,36]

$$K = \mu_0 M_s H_c/2 \quad (6)$$

$$H_a = 4|K|/3\mu_0 M_s \quad (7)$$

$$2\pi f_r = rH_a \quad (8)$$

where μ_0 stands for the universal value of permeability in free space ($4\pi \times 10^{-7}$ Hm^{-1}), r is the gyromagnetic ratio, and H_a is the anisotropy energy. From the equation, a high H_c value is related to a high k value, which results in a greater value of H_a. Finally, a high value of f_r is obtained.

DOI: 10.1021/acsami.5b01654
ACS Appl. Mater. Interfaces 2015, 7, 9776–9783

Figure 8 shows the calculated reflection loss value for the Co/CoO composites prepared under different temperatures. In

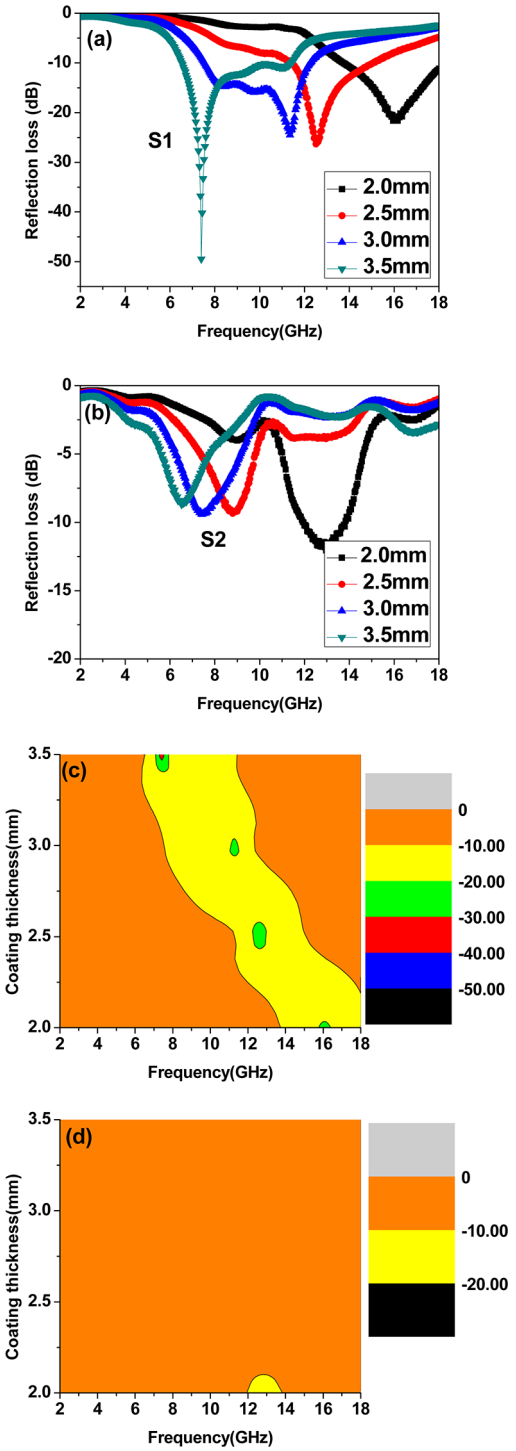

Figure 8. Reflection loss curves of the Co/CoO samples prepared at (a) 400 and (b) 500 °C and (c) the contour map of the RL_{min} ← 10 dB for the Co/CoO prepared at 400 °C (d) the contour map of the RL_{min} ← 10 dB for the Co/CoO prepared at 500 °C.

general, the RL_{min} value less than −10 dB is comparable to attenuate 90% of incident electromagnetic wave, and thus, the RL_{min} < −10 dB has been regarded as an ideal microwave absorption materials. It can be observed that the RL peaks of each composite shift to a lower frequency range as the increasing thickness. The shifting peaks can be explained by the $^1/_4$ wavelength equation.[37]

$$t_m = nc/4f_m(\varepsilon_r\mu_r)^{1/2} \quad (9)$$

where t_m and f_m represent for the matching thickness and frequency of the RL_{min} peaks, respectively, μ_r and ε_r are the complex permeability and permittivity, respectively, at matching frequency, and C is the velocity of light. Sample S1 has superior microwave absorption properties in both the RL_{min} value and frequency width as compared with S2. An optimal RL_{min} of −50 dB is obtained at 7.2 GHz for S1 with a coating thickness of 3.5 mm (Figure 8a). Moreover, when the composite has a thin coating thickness of 2 mm, sample S1 still exhibits the excellent microwave absorption properties, which the effective frequency bandwidth is up to 4.2 GHz (13.8−18 GHz) and the minimum reflection loss value reaches −22 dB. But for S2, the RL_{min} value cannot even reach −10 dB with a thickness of 2.5−3.5 mm. The best RL_{min} is just −12 dB with a coating thickness of 2 mm. From Figure 8c,d, we can conclude that S1 has a better microwave absorption property at identical coating thickness.

To investigate the probable mechanism for electromagnetic absorption performance, we displayed the electromagnetic parameters of the two composites in Figure 9. Actually, an absorbent with excellent microwave absorption may rely on the high impedance matching behavior, meaning the absorbent can let more and more electromagnetic wave incidence in it. For high impedance matching properties, material should meet the needs of the complex permeability and permittivity equally. Meanwhile, a big imaginary part of ε'' and μ'' value is also quite important and represents the attenuation ability of the electromagnetic wave. Figure 9a shows the real/imaginary permittivity value; S1 exhibits a relatively lower ε' value (6.5−8.7) and a large ε'' value (1−5.7), which may lead to not only poor impedance matching behavior but also strong electromagnetic attenuation. However, S2 has a better magnetic loss ability; both the real and imaginary parts of the permeability value are all slightly larger than those of S1 (Figure 9b) due to the increase of magnetic metal Co. From Figure 9c,d, we can conclude that the S1 has the stronger dielectric loss ability and a relatively weaker magnetic loss behavior. Hence, we introduce the attenuation constant α to describe the integral attenuation ability based on the following equation:[38]

$$\alpha = \frac{\sqrt{2}\pi f}{c} \times \sqrt{(\mu''\varepsilon'' - \mu'\varepsilon') + \sqrt{(\mu''\varepsilon'' - \mu'\varepsilon')^2 + (\mu'\varepsilon'' + \mu''\varepsilon')^2}} \quad (10)$$

where f is the frequency. It is clearly seen from Figure 9e that sample S1 presents a bigger attenuation constant value in the whole frequency range. In other words, the excellent microwave absorption properties of S1 are mainly attributed to the good impedance matching and strong dielectric loss.

As a result, we may conclude that the enhanced electromagnetic absorption may attribute to the following factors: (1) the relatively lower ε' value and big ε'' effectively increase the impedance matching properties. (2) S1 exhibits a stronger dielectric loss ability. As we know, the larger ε'' value is related to a lower ρ value based on the free electron theory ($\varepsilon''=1/\pi\varepsilon_0\rho f$).[39,40] However, the ρ value is affected by many factors including polarization, composition, morphology, and size. In this study, the weight ratio of S1 is slightly less than that of S2,

DOI: 10.1021/acsami.5b01654
ACS Appl. Mater. Interfaces 2015, 7, 9776−9783

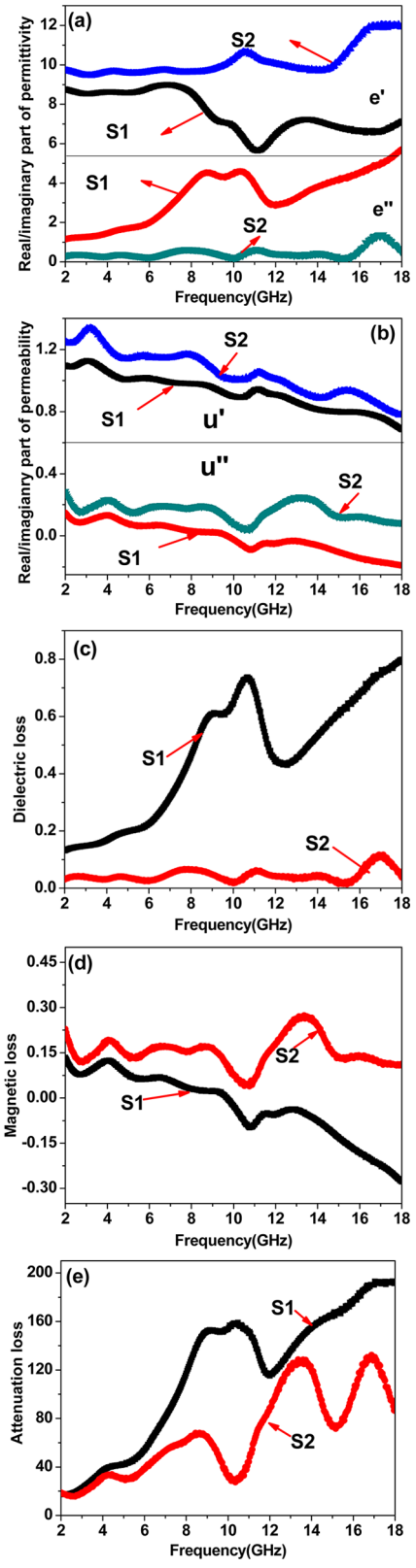

Figure 9. Electromagnetic parameters of the Co/CoO samples: (a) real/imaginary parts of permittivity, (b) real/imaginary parts of permeability, (c) dielectric loss; (d) magnetic loss; and (e) attenuation constant.

which can rule out the influence of the composite. Duan et al. have demonstrated that the dipole polarization is dominant.[41,42] The lattice defects caused by the difference of ionic radius (Co and CoO) serve as the polarized center. The dipoles need more and more energy to alternate the direction due to their damaged lattice structures. Such a process may increase the attenuation electromagnetic ability. (3) The porous 3-D flower structure with a larger layer spacing (300−600 nm) could lead to a multi-scatter among the leaves of the flower structure. What's more, the porous structures with a rough surface further increase the scattering intensity.

4. CONCLUSION

In this study, we designed a novel porous 3-D flower structure of Co/CoO by a simple heated treatment process. These 3-D flower structures present a porous feature with a pore diameter range of ∼25 nm. When the temperature is increased to 500 °C, the flower structures collapse due to the excessive reduction of CoO and result in the enlargement of the pore size, which causes them to collapse. The calculated reflection loss implies that the porous 3-D flower-like Co/CoO present attractive electromagnetic absorption properties. The effective frequency bandwidth is up to 11 GHz (7−18 GHz) with the coating thickness of 2 mm. Furthermore, the optimal frequency value for porous samples can reach −50 dB, higher than the −12 dB of the sample heated at 500 °C. The improved microwave absorption properties may come from the high impedance matching behavior and large ε''. Meanwhile, the special 3-D flower structure benefits electromagnetic wave scatter and results in enhanced microwave absorption properties.

AUTHOR INFORMATION

Corresponding Author

*E-mail: gbji@nuaa.edu.cn.

Notes

The authors declare no competing financial interest.

ACKNOWLEDGMENTS

Financial support from the Aeronautics Science Foundation of China (2014ZF52072), the National Natural Science Foundation of China (51172109 and 11475086), the Fundamental Research Funds for the Central University (no. 3082014NS2014057), and the Priority Academic Program Development of Jiangsu Higher Education Institutions is gratefully acknowledged.

REFERENCES

(1) He, Q. L.; Yuan, T. T.; Zhang, X.; Yan, X. R.; Guo, J.; Ding, D. W.; Khan, M. A.; Young, D. P.; Khasanov, A.; Luo, Z. P.; Liu, J. R.; Shen, T. D.; Liu, X. Y.; Wei, S. Y.; Guo, Z. H. Electromagnetic Field Absorbing Polypropylene Nanocomposites with Tuned Permittivity and Permeability by Nanoiron and Carbon Nanotubes. *J. Phys. Chem. C* **2014**, *118*, 24784−24796.

(2) Du, Y. C.; Liu, W. W.; Qiang, R.; Wang, Y.; Han, X.; Ma, J.; Xu, P. Shell Thickness-Dependent Microwave Absorption of Core−Shell Fe_3O_4@C Composites. *ACS Appl. Mater. Interfaces* **2014**, *6*, 12997−13006.

(3) Ren, Y. L.; Zhu, C. L.; Zhang, S.; Li, C. Y.; Chen, Y. J.; Gao, P.; Yang, P. P.; Ouyang, Q. Y. Three-dimensional SiO_2@Fe_3O_4 Core/Shell Nanorod Array/Graphene Architecture: Synthesis and Electromagnetic Absorption Properties. *Nanoscale* **2013**, *5*, 12296−12303.

(4) Lv, H. L.; Ji, G. B.; Wang, M.; Shang, C. M.; Zhang, H. Q.; Du, Y. W. FeCo/ZnO Composites with Enhancing Microwave Absorbing Properties: Effect of Hydrothermal Temperature and Time. *RSC Adv.* **2014**, *4*, 57529−57533.

(5) Liu, J. W.; Xu, J. J.; Che, R. C.; Chen, H. J.; Liu, M. M.; Liu, Z. W. Hierarchical Fe_3O_4@TiO_2 Yolk−Shell Microspheres with Enhanced

DOI: 10.1021/acsami.5b01654
ACS Appl. Mater. Interfaces 2015, 7, 9776−9783

Microwave-Absorption Properties. *Chem.—Eur. J.* **2013**, *19*, 6746−6752.
(6) Zong, M.; Huang, Y.; Wu, H. W.; Zhao, Y.; Wang, Q. F.; Sun, X. One-Pot Hydrothermal Synthesis of RGO/$CoFe_2O_4$ Composite and Its Excellent Microwave Absorption Properties. *Mater. Lett.* **2014**, *114*, 52−55.
(7) He, S.; Wang, G. S.; Lu, C.; Luo, X.; Wen, B.; Guo, L.; Cao, M. S. Controllable Fabrication of CuS Hierarchical Nanostructures and Their Optical, Photocatalytic, and Wave Absorption Properties. *ChemPlusChem.* **2013**, *78*, 250−258.
(8) Liu, J. R.; Itoh, M.; Terada, M.; Horikawa, T.; Machida, K. I. Enhanced Electromagnetic Wave Absorption Properties of Fe Nanowires in Gigaherz Range. *Appl. Phys. Lett.* **2007**, *91*, 093101−093103.
(9) Xia, F.; Liu, J. W.; Gu, D.; Zhao, P. F.; Zhang, J.; Che, R. C. Microwave Absorption Enhancement and Electron Microscopy Characterization of $BaTiO_3$ Nano-Torus. *Nanoscale* **2011**, *3*, 3860−3867.
(10) Guo, J. L.; Wang, X. L.; Miao, P. L.; Liao, X. P.; Zhang, W. H.; Shi, B. One-Step Seeding Growth of Controllable Ag@Ni Core−Shell Nanoparticles on Skin Collagen Fiber with Introduction of Plant Tannin and Their Application in High-Performance Microwave Absorption. *J. Mater. Chem.* **2012**, *22*, 11933−11942.
(11) Wang, T.; Wang, H. D.; Chi, X.; Li, R.; Wang, J. B. Synthesis and Microwave Absorption Properties of Fe−C Nanofibers by Electrospinning with Disperse Fe Nanoparticles Parceled by Carbon. *Carbon* **2014**, *74*, 312−318.
(12) Yan, L. G.; Wang, J. B.; Han, X. H.; Ren, Y.; Liu, Q. F.; Li, F. S. Enhanced Microwave Absorption of Fe Nanoflakes after Coating with SiO_2 Nanoshell. *Nanotechnology* **2010**, *21*, 095708.
(13) Ren, Y. L.; Zhu, C. L.; Qi, L. H.; Gao, H.; Chen, Y. J. Growth of γ-Fe_2O_3 Nanosheet Arrays on Graphene for Electromagnetic Absorption Applications. *RSC Adv.* **2014**, *4*, 21510−21516.
(14) Ji, R. L.; Cao, C. B.; Chen, Z.; Zhai, H. Z.; Bai, J. Solvothermal Synthesis of $Co_xFe_{3-x}O_4$ Spheres and Their Microwave Absorption Properties. *J. Mater. Chem. C* **2014**, *2*, 5944−5953.
(15) Zhao, B.; Shao, G.; Fan, B. B.; Chen, Y. Q.; Zhang, R. Effect of The TiO_2 Amounts on Microwave Absorption Properties of Ni/TiO_2 Heterostructure Composites. *Phys. B* **2014**, *454*, 120−125.
(16) Liu, J. W.; Cheng, J.; Che, R. C.; Xu, J. J.; Liu, M. M.; Liu, Z. W. Double-Shelled Yolk−Shell Microspheres with Fe_3O_4 Cores and SnO_2 Double Shells as High-Performance Microwave Absorbers. *J. Phys. Chem. C* **2013**, *117*, 489−495.
(17) Zhou, M.; Zhang, X.; Wei, J. M.; Zhao, S.; Wang, L. L.; Feng, B. X. Morphology-Controlled Synthesis and Novel Microwave Absorption Properties of Hollow Urchinlike α-MnO_2 Nanostructures. *J. Phys. Chem. C* **2011**, *115*, 1398−1402.
(18) Guan, H. T.; Xie, J. B.; Chen, G.; Wang, Y. D. Facile Synthesis of α-MnO_2 Nanorods at Low Temperature and Their Microwave Absorption Properties. *Mater. Chem. Phys.* **2014**, *143*, 1061−1068.
(19) Wu, R. B.; Zhou, K.; Yang, Z. H.; Qian, X. K.; Wei, J.; Liu, L.; Huang, Y. Z.; Kong, L. B.; Wang, L. Y. Molten-Salt-Mediated Synthesis of SiC Nanowires for Microwave Absorption Applications. *CrystEngComm* **2013**, *15*, 570−576.
(20) Fu, L. S.; Jiang, J. T.; Xu, C. Y.; Zhen, L. Synthesis of Hexagonal Fe Microflakes with Excellent Microwave Absorption Performance. *CrystEngComm* **2012**, *14*, 6827−6832.
(21) Sun, G. B.; Zhang, X. Q.; Cao, M. H.; Wei, B. Q.; Hu, C. W. Facile Synthesis, Characterization, and Microwave Absorbability of CoO Nanobelts and Submicrometer Spheres. *J. Phys. Chem. C* **2009**, *113*, 6948−6954.
(22) Zhang, X. K.; Ekiert, T.; Unruh, K. M.; Xiao, J. Q.; Golt, M.; Wu, R. X. High Frequency Properties of Polymer Composites Consisting of Aligned Fe Flakes. *J. Appl. Phys.* **2006**, *99*, 08M914−08M916.
(23) Deng, L. J.; Zhou, P. H.; Xie, J. L.; Zhang, L. J. Characterization and Microwave Resonance in Nanocrystalline FeCoNi Flake Composite. *Appl. Phys.* **2007**, *101*, 103916−103911.
(24) Wang, T.; Han, R.; Tan, G. G.; Wei, J. Q.; Qiao, L.; Li, F. S. Reflection Loss Mechanism of Single Layer Absorber for Flake-Shaped Carbonyl-Iron Particle Composite. *J. Appl. Phys.* **2012**, *112*, 104903−104908.
(25) Wang, Z. Z.; Zou, J. P.; Ding, Z. H.; Wu, J. F.; Wang, P. H.; Jin, S. W.; Bi, H. Magnetic and Microwave Absorption Properties of Ni Microcrystals with Hierarchical Branch-like and Flower-like Shapes. *Mater. Chem. Phys.* **2013**, *142*, 119−123.
(26) Feng, C.; Liu, X. G.; Sun, Y. P.; Jin, C. G.; Lv, Y. H. Enhanced Microwave Absorption of Flower-like FeNi@C Nanocomposites by Dual Dielectric Relaxation and Multiple Magnetic Resonance. *RSC Adv.* **2014**, *4*, 22710−22715.
(27) Yang, Z. H.; Li, Z. W.; Yu, L. H.; Yang, Y. H.; Xu, Z. C. Achieving High Performance Electromagnetic Wave Attenuation: A Rational Design of Silica Coated Mesoporous Iron Microcubes. *J. Mater. Chem. C* **2014**, *2*, 7583−7588.
(28) Hua, Z. H.; Deng, Y.; Li, K. N.; Yang, S. G. Low-Density Nanoporous Iron Foams Synthesized by Sol−Gel Autocombustion. *Nanoscale Res. Lett.* **2012**, *7*, 129−135.
(29) Sun, D. P.; Zou, Q.; Wang, Y. P.; Wang, Y. J.; Jiang, W.; Li, F. S. Controllable Synthesis of Porous Fe_3O_4@ZnO Sphere Decorated Graphene for Extraordinary Electromagnetic Wave Absorption. *Nanoscale* **2014**, *6*, 6557−6562.
(30) Lv, H. L.; Ji, G. B.; Wang, M.; Shang, C. M.; Zhang, H. Q.; Du, Y. W. Hexagonal-Cone like of $Fe_{50}Co_{50}$ with Broad Frequency Microwave Absorption: Effect of Ultrasonic Irradiation Time. *J. Alloy. Compds.* **2014**, *615*, 1037−1042.
(31) Bai, X.; Zhai, Y. B.; Zhang, Y. Green Approach to Prepare Graphene-based Composites with High Microwave Absorption Capacity. *J. Phys. Chem. C* **2011**, *115*, 11673−11677.
(32) He, C. Z.; Qiu, S.; Wang, X. Z.; Liu, J. R.; Luan, L. Q.; Liu, W.; Itoh, M.; Machida, K. I. Facile Synthesis of Hollow Porous Cobalt Spheres and Their Enhanced Electromagnetic Properties. *J. Mater. Chem.* **2012**, *22*, 22160−22166.
(33) Mandale, A. B.; Badrinarayanan, S.; Date, S. K.; Sinha, A. P. B. Photoelectron-Spectroscopic Study of Nickel, Manganese, and Cobalt Selenides. *J. Electron Spectrosc. Relat. Phenom.* **1984**, *33*, 61−67.
(34) Stevens, G. C.; Edmonds, T. Catalytic Activity of The Basal and Edge Planes of Molybdenum Disulphide. *J. Less-Common Mater.* **1977**, *54*, 321−329.
(35) Lv, H. L.; Liang, X. H.; Cheng, Y.; Ji, G. B.; Tang, D. M.; Zhang, B. S.; Zhang, H. Q.; Du, Y. W. Facile Synthesis of Porous Coin-like Iron and Its Excellent Electromagnetic Absorption Performance. *RSC Adv.* **2015**, *5*, 25936−25941.
(36) Lv, H. L.; Liang, X. H.; Cheng, Y.; Zhang, H. Q.; Tang, D. M.; Zhang, B. S.; Ji, G. B.; Du, Y. W. Coin-like α-Fe_2O_3@$CoFe_2O_4$ Core-Shell Composites with Excellent Electromagnetic Absorption Performance. *ACS Appl. Mater. Interfaces* **2015**, *7*, 4744−4750.
(37) Li, G. M.; Wang, L. C.; Li, W. X.; Ding, R. M.; Xu, Y. $CoFe_2O_4$ and/or Co_3Fe_7 Loaded Porous Activated Carbon Balls as a Lightweight Microwave Absorbent. *Phys. Chem. Chem. Phys.* **2014**, *16*, 12385−12392.
(38) Zhao, B.; Shao, G.; Fan, B. B.; Zhao, W. Y.; Zhang, R. Investigation of the Electromagnetic Absorption Properties of Ni@TiO_2 and Ni@SiO_2 Composite Microspheres with Core−Shell Structure. *Phys. Chem. Chem. Phys.* **2015**, *17*, 2531−2539.
(39) Liu, X. G.; Geng, D. Y.; Meng, H.; Shang, P. J.; Zhang, Z. D. Erratum: Microwave-Absorption Properties of ZnO-Coated Iron Nanocapsules. *Appl. Phys. Lett.* **2008**, *92*, 17317−17319.
(40) Wu, H.; Wang, L. D.; Wu, H. J.; Lian, Q. Synthesis and Significantly Enhanced Microwave Absorption Properties of Hematite Dendrites/Polyaniline Nanocomposite. *Appl. Phys. A: Mater. Sci. Process.* **2014**, *115*, 1299−1307.
(41) Duan, Y. P.; Liu, Z.; Jing, H.; Zhang, Y. H.; Li, S. Q. Novel Microwave Dielectric Response of Ni/Co-Doped Manganese Dioxides and Their Microwave Absorbing Properties. *J. Mater. Chem.* **2012**, *22*, 18291−18299.
(42) Duan, Y. P.; Liu, Z.; Zhang, Y. H.; Wen, M. A Theoretical Study of The Dielectric and Magnetic Responses of Fe-Doped α-MnO_2

DOI: 10.1021/acsami.5b01654
ACS Appl. Mater. Interfaces 2015, 7, 9776−9783

Based on Quantum Mechanical Calculations. *J. Mater. Chem. C* **2013**, *1*, 1990−1994.

DOI: 10.1021/acsami.5b01654
ACS Appl. Mater. Interfaces 2015, 7, 9776−9783